APPLIED PHYSICS

An electrically pumped phonon-polariton laser

Keita Ohtani*, Bo Meng, Martin Franckié*, Lorenzo Bosco, Camille Ndebeka-Bandou, Mattias Beck, Jérôme Faist*

We report a device that provides coherent emission of phonon polaritons, a mixed state between photons and optical phonons in an ionic crystal. An electrically pumped GaInAs/AlInAs quantum cascade structure provides intersubband gain into the polariton mode at λ = 26.3 μm, allowing self-oscillations close to the longitudinal optical phonon energy of AlAs. Because of the large computed phonon fraction of the polariton of 65%, the emission appears directly on a Raman spectrum measurement, exhibiting a Stokes and anti-Stokes component with the expected shift of 48 meV.

INTRODUCTION

The polariton, a mixed state between a photon and an electronic excitation in solid-state matter, has recently attracted much attention due to its rich physics that includes superfluidity, quantized vortices, and Bose-Einstein condensation (*1*, *2*). In addition, the possibility of engineering both the optical and matter parts of this quasiparticle can be exploited for the creation of polaritonic devices with enhanced nonlinear properties (*3*–*5*). An exciton-polariton laser created using a semiconductor microcavity is an elegant example since it reaches the threshold by stimulated scattering of the polaritons (*6*, *7*) instead of population inversion between conduction and valence band states. Other functional polaritonic devices are also investigated using other material elementary excitations (*8*–*11*). The phonon is the elementary excitation of lattice vibrations in a solid; in an ionic crystal, its optical mode is strongly coupled with light, leading to the formation of a phonon polariton (*12*, *13*). As vibration frequencies of many polar materials lay in the terahertz (THz) spectral region, the excitation and emission of these polaritons from a near-infrared source via a nonlinear interaction have attracted much interest (*14*, *15*), including its use in THz spectroscopy applications (*15*). In addition, the phonon polariton displays very peculiar features of coherent emission and propagation (*16*, *17*), in its waveguiding (*18*), coupling to metamaterial resonators (*19*), and tunable resonant energy scaled down to a few atomic layers in two-dimensional materials (*20*). Control and manipulation of these properties open up the possibilities to build a platform based on solid-state materials to explore THz nanophotonics and nanophononics.

In contrast to optical pumping of phonon polaritons, electrical pumping, desirable for numerous applications, remains a challenging task. Here, we report the demonstration of an electrically pumped phonon-polariton semiconductor laser. A suitably engineered semiconductor quantum well heterostructure is electrically excited and provides gain mainly into the photon fraction of the phonon polariton. As a result, phonon-polariton lasing action at an energy close to the longitudinal optical (LO) phonon energy ($\hbar\omega_{LO}$) with a phonon fraction of 65% is achieved.

As illustrated in Fig. 1, phonon polaritons are generated in our structure in the quantum cascade active region based on an InGaAs/AlInAs heterostructure (*21*) (the computed electron band structure is shown in Fig. 1C). In this work, we targeted the AlAs transverse optical (TO) phonon in the AlInAs barrier layers at $\hbar\omega_{TO} \approx 42$ meV because it is energetically well separated from the frequency of the other TO phonons (InAs, $\hbar\omega_{TO} \approx 29$ meV; GaAs, $\hbar\omega_{TO} \approx 31$ meV), allowing it to be selectively excited. The active region, based on a bound-to-continuum transition scheme (*22*), is designed to provide gain mainly into the photon fraction of the polariton at $\hbar\omega_{TO}$ of AlAs by our density matrix simulator (*23*). In addition, recent theoretical results show that, depending on the frequency, the phonon fraction will also experience a gain of approximately 1 to 10% of the one experienced by the photon fraction (*24*). This has been confirmed for the present design by computing the phonon-polariton emission rate using Fermi's golden rule and a nonequilibrium Green's function transport model (*25*). Although the intersubband laser transition energy is 43.7 meV, due to the polaritonic nature of the emitted radiation, the laser is expected to operate at 48.2 meV. The cavity thus favors a greater phonon component of the polariton, resulting in a nonphotonic fraction of the emission rate of 7% (at the experimental lasing energy of 47.2 meV, it is 10%). Waveguiding of the phonon polaritons is performed in a hybrid way, as the phonon excitation is naturally confined within the AlInAs layers, while the photonic part is guided along the plane of the layers by the two metallic contact layers (*26*) shown in Fig. 1A. As shown by the calculated polariton energy density displayed in Fig. 1B, about half of the electromagnetic energy is concentrated in the barrier material in a deep subwavelength dimension.

RESULTS

To provide an unambiguous probe of the phonon-polaritonic nature of the emission, we used both a direct measurement of the optical emission at THz frequencies and Raman scattering with a green light excitation. Furthermore, we indirectly measured the polariton dispersion by combining the emission spectra at a wide range of wavelengths. For the experiment, a 4.1-μm-thick structure composed of 60 repetitions of the proposed active region was grown by molecular beam epitaxy on InP substrates. To observe the subthreshold emission spectra (T = 10 K), we measured a short device using a home-built vacuum Fourier transform infrared spectrometer (FTIR) equipped with a He-cooled Si bolometer. As seen in Fig. 2A, the emission spectra display an asymmetric shape, with two sharp maxima, separated by the energy gap formed between the two AlAs LO and TO optical phonon energies, which were determined by Raman scattering (Fig. 2B) and far-infrared transmission measurements (Fig. 2C), respectively. Lasing occurs at a photon energy of 47.2 meV, which is slightly higher than $\hbar\omega_{LO}$ of AlAs. The light intensity versus injected current curve (shown in Fig. 2D)

Institute for Quantum Electronics, ETH Zürich, August-Piccard-Hof 1, 8093 Zurich, Switzerland.
*Corresponding author. Email: keitaohtani@gmail.com (K.O.); martin.franckie@phys.ethz.ch (M.F.); jerome.faist@phys.ethz.ch (J.F.)

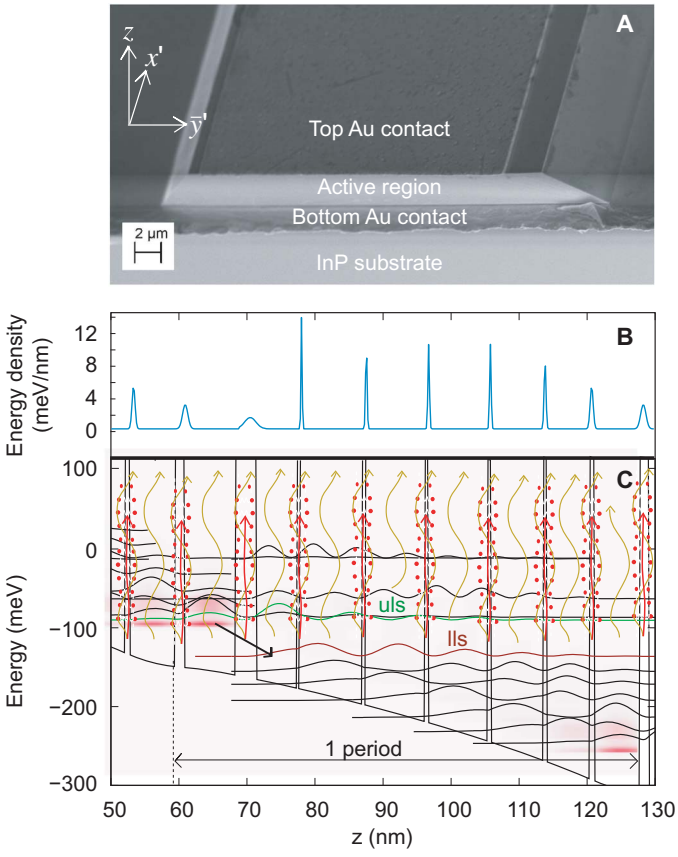

Fig. 1. Schematics and design of the device structure. (**A**) Scanning electron microscopy picture of the phonon-polariton laser consisting of an active region based on 60 periods of the structure shown in (C) inside a double-metal cavity formed by the top and bottom contacts. (**B**) Phonon-polariton energy density along the growth direction (*z*). Most of the energy is concentrated in the barriers where the phonon part of the polariton is confined, while the photon part contributes with an approximately constant energy density. For the computed case with a phonon fraction of 0.5, each constituent makes up about half of the total polariton energy integrated over one period. (**C**) Band structure diagram of the phonon-polariton laser design (called EV2128), where the gain transition from the upper laser state (uls) to the lower laser state (lls) is indicated. The phonon and photon constituents, traveling in the plane of the laser, are schematically drawn. The color scale shows the electron density computed with a nonequilibrium Green's function model at 100-K lattice temperature and shows an inverted population at the plotted bias (19 kV/cm).

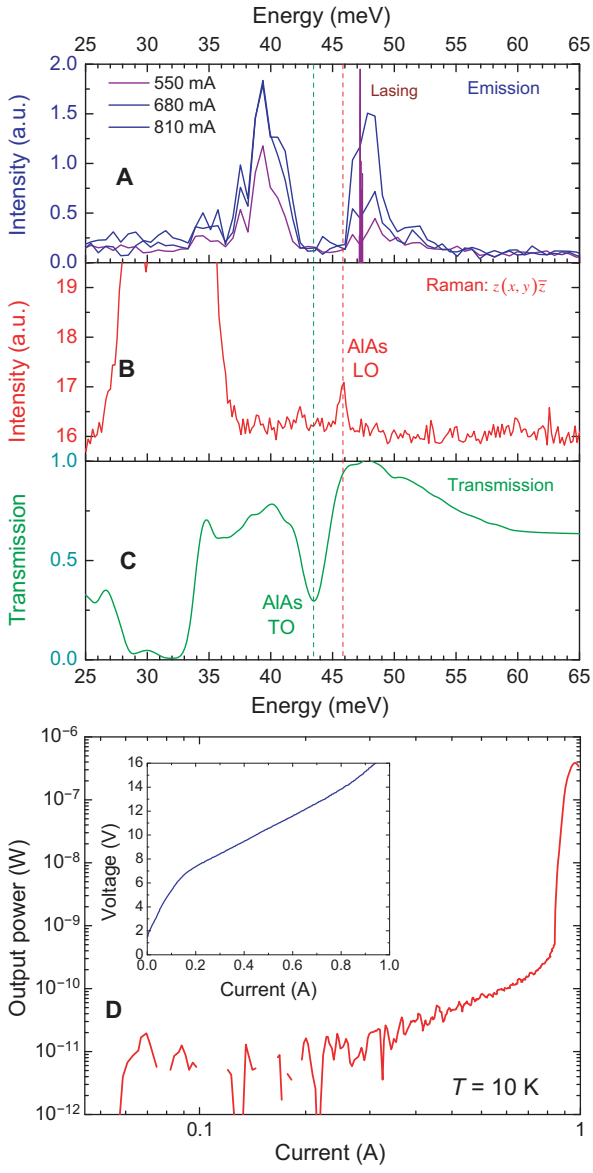

Fig. 2. Device characteristics. (**A**) Measured subthreshold emission spectra ($T = 10$ K). Two peaks separated by the AlAs reststrahlen band were observed, stemming from the emission from the lower and upper phonon-polariton branches, respectively. The low-temperature laser spectrum at 880 mA is also shown. a.u., arbitrary units. (**B**) Measured Raman spectrum taken from the active region in the $z(x,y)\bar{z}$ geometry. (**C**) Room-temperature direct transmission spectrum using a room-temperature deuterated triglycine sulfate detector. (**D**) Light output versus current characteristic. A single threshold current (=880 mA) was observed. The inset shows the transport curve of the device. The ridge width of the device is ~30 μm, and the length was 250 μm.

exhibits a single threshold behavior. We attribute the absence of a double threshold, usually seen in exciton-polariton lasers, to the different nature of the material excitations: Whereas the bosonic nature of phonons is independent of their population, excitons will ionize at high densities into a free electron and hole gas (*6*, *7*, *27*, *28*), leading to a second threshold.

Next, to probe the phonon constituent of the polariton, we measured the low-temperature ($T = 5$ K) micro–Raman scattering spectra of a 300-μm-long and 30-μm-wide quantum cascade structure under operation. To limit the dissipation, we drove the device at a 10% duty cycle. A polarized continuous-wave green laser light with a wavelength of $\lambda = 532$ nm was focused on the cleaved facet of the laser, and the back-scattered light was measured through a grating-based spectrometer. As depicted in Fig. 3A, for the laser driven below the threshold ($I = 670$ mA), the spectrum was consistent with the phonon peaks associated with the InGaAs/AlInAs layers. In particular, we assigned the peaks at 28 and 32 meV to the InAs and GaAs TO phonons, respectively. However, a peak appears both in the Stokes and anti-Stokes sides at an energy corresponding exactly to the energy of the phonon polariton when the device is driven above the threshold ($I = 1050$ mA). While for the TO phonon peaks, the ratio of the anti-Stokes to Stokes sideband intensity is 0.42 and corresponds to a thermal phonon population at a temperature of ~150 K mainly caused by localized heating from the $P = 20$ mW green laser spot (assuming a constant Raman cross section and taking the InAs TO phonon), and the same ratio is close to unity for the polaritonic peak.

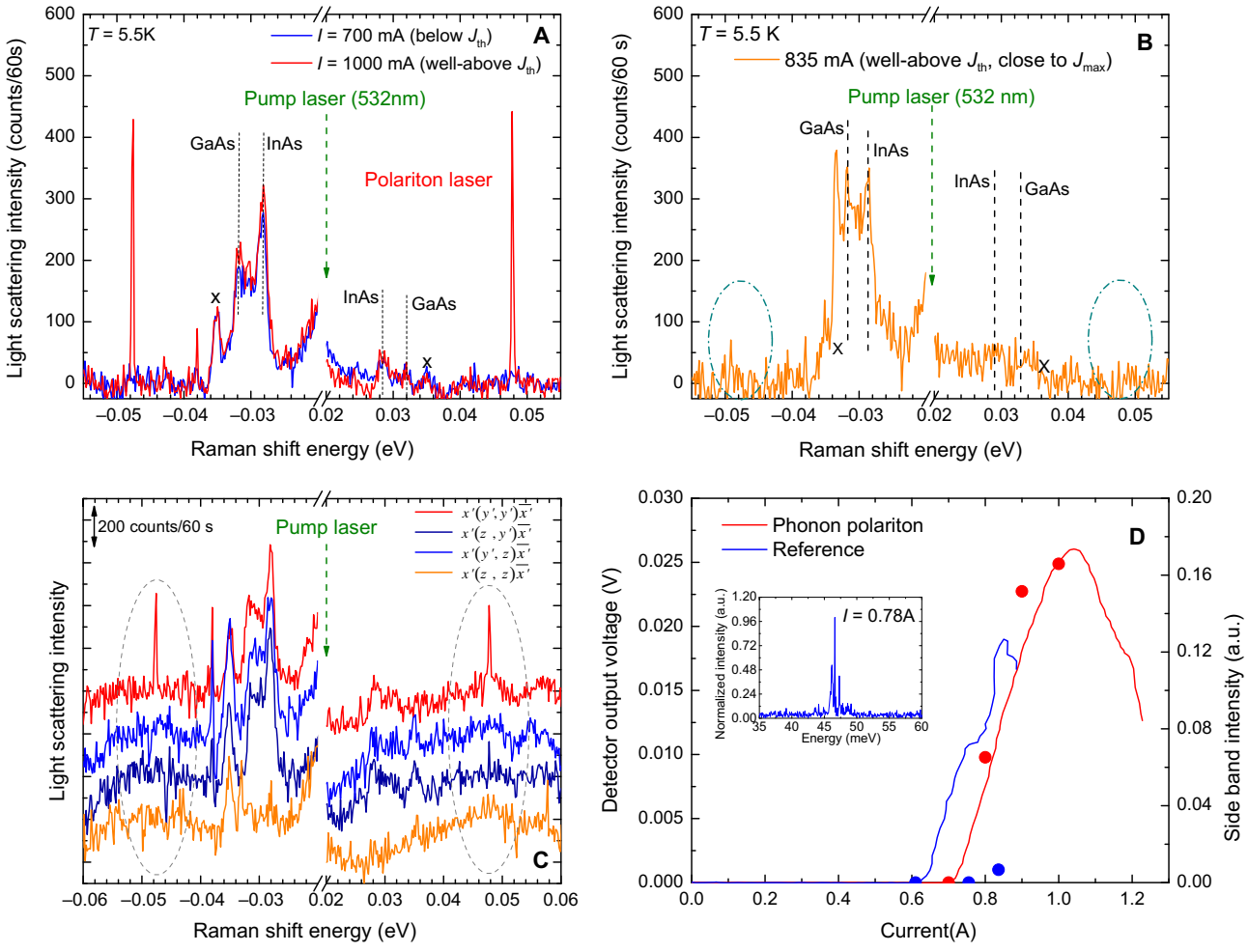

Fig. 3. Raman spectroscopy of the phonon-polariton laser and the reference laser with GaAaSb barriers. (**A**) Low-temperature (T = 5.5 K) polarized Raman scattering spectra of the facet of the phonon-polariton laser under operation. The peaks at 28 and 32 meV are attributed to the InAs and GaAs phonons of the active region, respectively. The peak at 35 meV, denoted by "x," is an artifact attributed to the Raman scattering inside the optics used in the setup. The phonon-polariton peak at 48 meV is seen when the device is driven above the threshold (1060 mA) and disappears when the device is below the threshold (670 mA). (**B**) Raman spectrum of the reference sample at a current of 835 mA, which is close to the roll-over current of the device. (**C**) Polarization selection rules for the phonon-polariton peak, which appears only for the in-plane polarization combination [$x'(y', y')\bar{x}'$]. (**D**) Light and Raman sideband intensity of the phonon polariton and the reference devices as function of the injected current. The inset shows the lasing spectrum of the reference sample (EP1562).

This is expected as the occupancy of the phonon polariton is well above unity above the threshold. Under the driving conditions considered in this experiment, we estimated a population on the order of approximately 10^5 polaritons. We attributed the small strength of the polaritonic signal, also responsible for the fact that the phonon polaritons are not observed below the threshold, to the fact that the Raman emission in backscattering is normally forbidden by the momentum selection rule, because of the very small momentum carried by the phonon polariton. Emission is still detected because of the very short penetration length of the pump laser. Shown in Fig. 3B is the Raman backscattering spectra obtained for a laser where the active region consisted of a reference laser heterostructure where the AlInAs barriers were substituted by GaAsSb ones. These devices do not contain any AlInAs material but exhibit a similar intersubband gain coefficient (*29*). Although the laser emitted at roughly the same frequency, in the Raman shift region where the phonon-polariton signal is expected, only a faint peak is visible just above the noise. This behavior is expected as a consequence of the weak photon-phonon coupling caused by the large detuning of the cavity mode from the closest TO phonon line of GaAs at 32 meV and was also observed in a reference 3-THz quantum cascade laser (QCL) under operation as shown in fig. S5.

The Raman selection rules can be derived from the Raman tensors (see section S7). For phonon modes polarized along the growth direction, only the $x'(y', y')\bar{x}'$ configuration can provide a Raman signal, and for modes with in-plane polarization, only the cross-polarization combinations $x'(y', z)\bar{x}'$ and $x'(z, y')\bar{x}'$ can occur. Thus, as shown in Fig. 3C, the Raman signal for the mode at the phonon-polariton frequency [with signal only for $x'(y',y')\bar{x}'$] shows that this mode is extremely polarized along the growth direction, while the phonon modes of GaAs and InAs are unpolarized [with signal for the cross and the $x'(y', y')\bar{x}'$ combinations], as expected, since the polariton is strongly coupled to the vertically polarized cavity mode.

It is true for any QCLs operating at THz frequencies that a portion of the electromagnetic energy is stored in the phonon modes of the host material. However, one cannot expect stimulated emission of polaritons in those situations since the emission energy is sufficiently far from the anticrossing point so that the dispersion is linear (see fig. S5). We were not able to observe the Raman signals from InGaAs/AlInGaAs THz

QCLs emitting at 15 meV that is well separated from the InAs and the GaAs TO phonon energy. In our device, the situation is markedly different as the dispersion is highly nonlinear, making it possible for the electrons to undergo stimulated emission directly into a polariton mode with a predominant phonon fraction, as shown in the following. First, Fig. 3D compares the intensity of the Raman peak and the light power as a function of the injected current for the polariton and the reference devices. In the device with the AlInAs barrier layers, the Raman peak linearly follows the intensity of the measured laser signal, in agreement with the fact that both emissions originate from the same phonon polariton stimulatively emitted by the intersubband electrons. Second, to quantify the polaritonic dispersion of the emission, we also grew six additional structures in which the gain is designed to peak at different energies higher than $\hbar\omega_{TO}$ of AlAs, between 47 and 53 meV (see the Supplementary Materials for their active region designs). The high-resolution ($\Delta\nu$ = 0.015 meV) optical spectra of these Fabry-Pérot (FP) lasers of fixed cavity lengths (1 mm, cleaving length error within 10 μm) are reported in Fig. 4A. Here, it is evident that the longitudinal mode spacing rapidly shrinks in a very small photon energy range (≈5 meV). In contrast to the case of the exciton polaritons, where the dispersion $\omega(k)$ of the polaritons is measured directly by angle-dependent photoluminescence (*30*), we use an approach to retrieve the group refractive index $n_g(\omega) = c\,(\partial k/\partial\omega)$, which is a measure of its inverse derivative. n_g is experimentally retrieved from the angular frequency spacing $\Delta\omega$ of the longitudinal modes of the FP cavity using $n_g = c/v_g = \pi c/(L\Delta\omega)$, where c is the light velocity and v_g is the group velocity, and is plotted by red circles in Fig. 4B. Here, we also compare the experimental results to the prediction of a theoretical model (described in section S4), in which the light-matter coupling is studied in the dipole gauge and the quadratic term of the vector potential appears as a polarization self-interaction (*24*, *31*). The group index exhibits a very strong frequency dependence, changing by a factor of two within 2 meV. This highly dispersive n_g is expected for a phonon polariton, arising from the "slowing down" of the group velocity as the upper polariton branch departs from the light line and converges to the pure phonon excitation. In contrast, the blue symbols in Fig. 4B that report the group index n_g of the reference QCLs with GaAsSb barriers that were designed for 46- and 49-meV emission show a flat dispersion. The comparison between these two characteristics shows that the strong dispersion observed in the group index n_g must be predominantly attributed to the presence of the AlAs optical phonon and that the contribution of the intersubband gain is negligible. As a comparison, we also report by a dashed line in Fig. 4B the predictions of a classical model that treats the active region as a quasi-bulk material and whose details are reported in section S2 (*32*). This approach completely fails to correctly predict the experimental data. The excellent agreement between the computed dispersion of n_g and the measured one is further evidence of the polaritonic nature of the emission.

In Fig. 4C, the measured emission energies are plotted onto the computed upper branch of the phonon-polariton dispersion. From their wave vectors, the phonon and photon fraction of the polaritons can be derived from the Hopfield coefficients α_{photon} and α_{phonon} (with $\alpha_{photon} + \alpha_{phonon} = 1$) (*31*, *33*), as shown in Fig. 4D, a phonon fraction as high as α_{phonon} = 65% is inferred.

DISCUSSION

The fact that the lasing is observed on the Raman scattering spectra is a strong indication of the phonon-polariton nature of the emitted radiation. While the creation of sidebands on a near infrared carrier has been

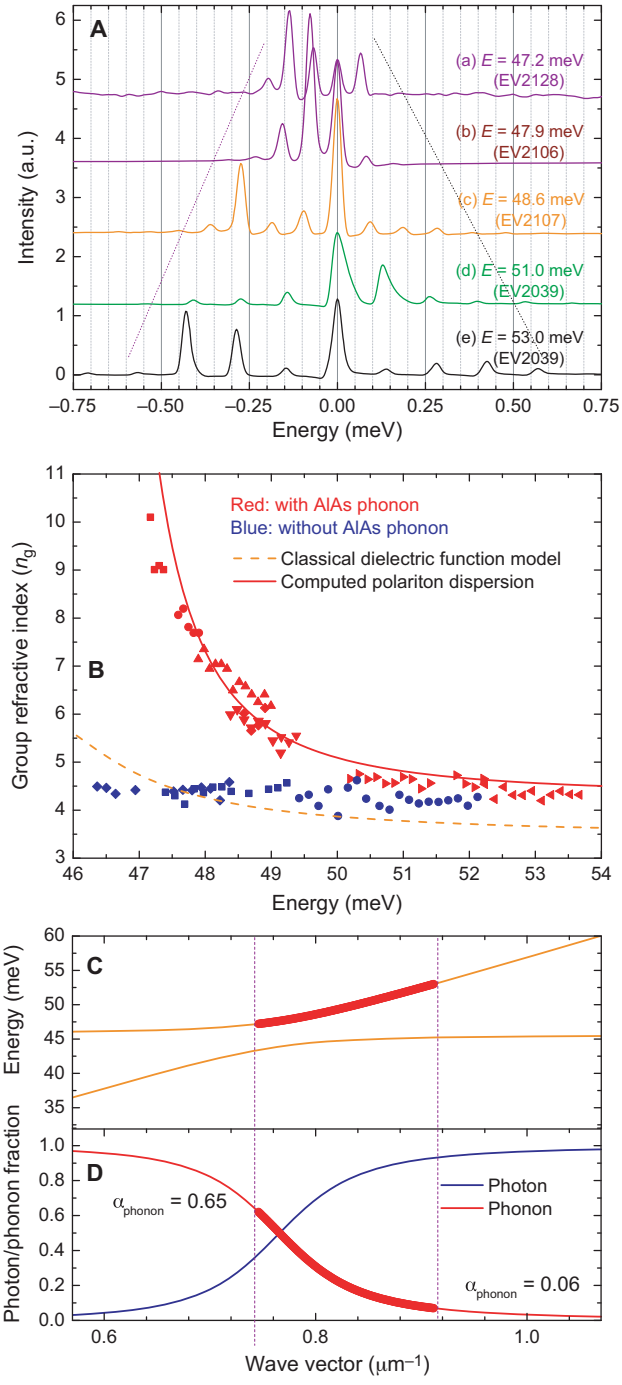

Fig. 4. Phonon-polariton laser emission spectra. (**A**) High-resolution emission spectra of the FP devices. The cavity length of all the devices was fixed at 1.0 mm. The longitudinal mode spacing is strongly reduced when the laser emission energy approaches to the AlAs optical phonon energy. The spectral measurements were performed at T = 15 K. (**B**) Group refractive index (n_g) retrieved from the longitudinal mode spacing of the FP devices. The red solid points represent n_g of the FP devices containing the AlAs phonon oscillators, while the group index n_g of the FP devices without the AlAs phonon oscillators are depicted by the blue solid points (the symbols represent different samples as given in the Supplementary Materials). The red solid line shows n_g derived from the computed phonon-polariton dispersion. (**C**) Computed phonon-polariton dispersion for our laser devices. The red circles represent the emission energies of the measured devices in (B). (**D**) Computed Hopfield coefficients. In this model, a phonon fraction of 0.65 is obtained at the lowest emission energy (47.2 meV).

reported previously, the effect was either based on the bulk GaAs $\chi^{(2)}$ nonlinearity using long interaction length and a careful phase matching (*34*) or based on a resonant near-infrared excitonic nonlinearity (*35*). In contrast, in our case, the interaction length is very short (<0.5 μm), and the laser is detuned. The Raman scattering is a consequence of the large phonon component of the polaritons and the large resulting optical nonlinearity at the polariton energy. The large phonon component of the polariton is also responsible for the very steep dispersion of the emission that translates into a very strong energy dependence of the group index.

In our polariton laser, the threshold is reached when the overall polariton gain, the sum of its photon and phonon components (*24*), equals the losses. The polariton lifetime can be written in terms of the weighted content of the photon and phonon parts

$$1/\tau_{\text{polariton}} = \alpha_{\text{photon}}/\tau_{\text{cavity}} + \alpha_{\text{phonon}}/\tau_{\text{phonon}} \quad (1)$$

Considering the values for the device operating at an energy of 47.2 meV, with the maximum phonon fraction of 0.65, we evaluate for the cavity a value τ_{cavity} = 1.7 ps, taking into account absorption losses by the metal and the active region. The width of the TO phonon Raman peak strongly depends on the angle of the extracted light (*36*) and therefore does not reflect the lifetime broadening in our setup. Taking only the intrinsic broadening (*36*), we obtain $\tau_{\text{polariton}}$ = 3.2 ps, corresponding to an energy broadening of 0.2 meV. The latter is one order of magnitude smaller than the Rabi coupling energy (Ω_R = 2.0 meV), justifying the existence of the polariton description even in the absence of gain, in contrast to our previous results reported in (*37*).

It is important to stress that, because the polariton lifetime is a weighted average in devices that exhibit short-photon and long-phonon lifetimes, the performance of phonon-polariton lasers can be expected to be better than the one of the normal laser because the former benefit from the pure phonon gain (*24*). As shown in detail in section S6, with one exception, our devices have maximum operating temperatures between 170 and 215 K that are roughly equivalent to the ones of the reference material (T_{max} from 190 to 205 K). An optimized phonon-polariton would have the barriers containing AlAs close to the upper state wave function for maximum phonon gain and not in the injection barrier where they are only passive. In addition, the use of binary AlAs barriers without alloy disorder would exhibit a much narrower theoretically predicted phonon linewidth (*38*) and would further lower the threshold.

In conclusion, we have demonstrated the first electrically pumped phonon-polariton laser. Our claim is supported by the direct observation of the photon, phonon, and polariton signatures of the emission. Specifically, we have measured the photon emission into a laser mode close to the AlAs LO phonon frequency, a highly nonthermal phonon population at the laser frequency above, but not below, laser threshold, and a highly frequency-dependent group index, which matches very well the one predicted from a phonon-polariton dispersion and strongly deviates from that of a classical model. Last, our simulations of the phonon-polariton emission rate show a peak at a frequency close to the observed laser frequency and a similar threshold current density to the experimental one. A unique feature of this laser is that a large fraction of the energy of the emitted "light" is carried in the mechanical motion of the atoms and this device can therefore be seen as a version of a phonon laser. Because of their bosonic nature, it is legitimate to consider a laser-like process in which a coherent population of phonons with an occupation number much larger than one is created and maintained by pumping. The first implementation of such an idea used as phonon modes the mechanical excitations of the Mg^+ ion in a trap potential (*39*). Using an optomechanical platform, a phonon laser operating at a phonon frequency of 21 MHz was demonstrated by optical pumping. A pure mechanical phonon laser operating at 100 kHz has also been achieved recently using a piezoelectric excitation of a micromechanical resonator (*40*). Much higher frequencies, achieved using optical phonons of solids, have also been considered (*41*, *42*). However, as was pointed out by Chen and Khurgin (*41*), the very large optical phonon density of states makes the realization of these optical phonon lasers difficult as all the modes of the resonator within the energy range of the gain must be populated until the threshold is reached for the mode with the large gain and lower losses. In the work presented here, the use of phonon polaritons alleviates this problem as the coupling of the phonon to the photon effectively decreases the density of states close to the anticrossing point, thus reducing the threshold current density. The effect is similar to the one observed in microcavities, where the coupling of the exciton to the cavity mode reduces their mass and enables their condensation. Last, because the energy is partially stored in the form of phonons that have a relatively long lifetime and are naturally confined within nanometer-thick layers, phonon-polariton lasers could be operated with extremely small cavity sizes that would maintain higher quality factors than the one possible with plasmonics (*43*). As a result, the design concept explored here would be very well suited for applications based on two-dimensional van der Waals materials, where low-loss boron nitride phonons could provide the phonon-polariton mode (*44*).

MATERIALS AND METHODS

Materials

The samples were grown by molecular beam epitaxy on Fe-doped InP (001) substrates, starting with a 60-nm-thick $In_{0.53}Ga_{0.47}As$ buffer layer. Then, a 4.1-μm-thick active region was deposited, and the growth was completed by a 15-nm-thick Si-doped n-type $Ga_{0.53}In_{0.47}As$ contact layer ($n = 5.0 \times 10^{18}$ cm^{-3}). In the active region, the following layer structure (EV2128) was repeated 60 times: in nanometers, **3.0**/6.0/**0.3**/9.3/**0.4**/8.9/**0.4**/8.8/**0.4**/7.7/**0.5**/6.3/**0.8**/6.6/**1.4**/7.5, where $Al_{0.48}In_{0.52}As$ barrier layers are in bold, $In_{0.53}Ga_{0.47}As$ well layers are in roman, and the Si-doped $In_{0.53}Ga_{0.47}As$ layer ($n = 4.1 \times 10^{17}$ cm^{-3}) is underlined. All the layer structures presented here are summarized in table S1. The corresponding conduction band diagram of the one period of the active region with moduli-squared relevant wave functions is also shown in fig. S1.

Methods

For laser device fabrication, a bottom metal contact layer composed of a 10-nm-thick titanium (Ti) and a 500-nm–thick gold (Au) was first deposited on the grown wafer. It was wafer-bonded onto the Au-evaporated *n*-InP (100) carrier substrate by thermocompression bonding technique. Then, the Fe-doped InP substrate used for the epitaxial growth was removed by mechanical polishing and selective wet chemical etching. After evaporation of a 260-nm-thick Ti/Au top contact, the ridge laser structures were defined by a wet chemical etching. After device fabrication, the processed wafer was cleaved into 0.25- to 1.0-mm-long FP lasers with a ridge width of 30 μm and then mounted on copper mounts. The laser devices were placed in a temperature-controlled He flow cryostat with KRS5 vacuum windows.

For the low-temperature (T = 5 K) micro–Raman scattering experiment, a continuous-wave frequency doubled Nd:YAG (wavelength, 532.1 nm) laser was focused through the cryostat window into a 2.5-μm-diameter spot by a ×50 objective lens with a numerical aperture of 0.4. Backward-scattered light was collected and sent to the single-grating monochrometer equipped with a LN_2-cooled Si charge-coupled device (CCD) detector. According to the Raman scattering selection rule for a zinc blende crystal, $z(x,y)\bar{z}$ and $x'(z,y')\bar{x}'$ geometries were used for LO and TO phonons, respectively (*45*). Here, z denotes the [001] axis, which is parallel to the InP substrate surface (001) (crystal growth direction), and $x(y)$ is along the direction of [100]([010]). In addition, x' and y' denote the $[1\bar{1}0]$ and the [110] axes, respectively. The power of the laser was varied from 5 mW to a maximum of 20 mW, limited by local heating at the focal point.

To determine the AlAs TO phonon energy, a normal incident light transmission was measured. The active region film was glued on a Si substrate. To compensate the temperature difference of the two experiments, the transmission spectrum was shifted by 0.8 meV, which is consistent with the temperature-induced energy shift of the LO phonon energy as measured by Raman scattering experiment.

The subthreshold electroluminescence measurements (T = 10 K) were performed using a home-made vacuum FTIR equipped with a calibrated Si bolometer. A current pulse train composed of 100-ns-wide pulses with a repetition rate of 1 MHz (a duty cycle of 10%) was modulated at 450 Hz to match the frequency response of the calibrated Si bolometer. The light output power was also measured by the Si bolometer. For high-resolution spectral measurements, a Bruker vacuum FTIR was used. To minimize the broadening of the spectra, the length of the electrical pulses was kept below 50 ns. The spectral resolution used in this study was 0.125 cm^{-1}.

SUPPLEMENTARY MATERIALS

Supplementary material for this article is available at http://advances.sciencemag.org/cgi/content/full/5/7/eaau1632/DC1

Supplementary Text

Fig. S1. Conduction band diagrams.

Fig. S2. Characteristics of the first order distributed feedback lasers and the FP lasers of the reference InGaAs/GaAsSb structure.

Fig. S3. Nonequilibrium Green's function simulation results.

Fig. S4. Phonon-polariton dispersion (red) and lower polariton Hopfield coefficients of the phonon ($h_{phon.}$) and photon ($h_{phot.}$) components for a 4.7-THz GaAs/AlGaAs QCL (*53*).

Fig. S5. Raman spectroscopy of the four-well InGaAs/AlInGaAs QCL emitting at 3.6 THz.

Table S1. Layer structures and properties of all the grown samples.

Table S2. Selection rules for Raman backscattering from TO phonon modes polarized along the y' or z directions, as well as LO phonon modes.

References (*46*–*53*)

REFERENCES AND NOTES

1. I. Carusotto, C. Ciuti, Quantum fluids of light. *Rev. Mod. Phys.* **85**, 299–366 (2013).
2. J. Kasprzak, M. Richard, S. Kundermann, A. Bass, P. Jeambrun, J. M. J. Keeling, F. M. Marchetti, M. H. Szymańska, R. André, J. L. Staehli, V. Sanova, P. B. Littlewood, B. Deveaud, L. S. Dang, Bose-Einstein condensation of exciton polaritons. *Nature* **443**, 409–414 (2006).
3. D. Sanvitto, S. Kéna-Cohen, The road towards polaritonic devices. *Nat. Mater.* **15**, 1061–1073 (2016).
4. D. Ballarini, M. De Giorgi, E. Cancellieri, R. Houdré, E. Giacobino, R. Cingolani, A. Bramati, G. Gigli, D. Sanvitto, All-optical polariton transistor. *Nat. Commun.* **4**, 1778 (2013).
5. C. Sturm, D. Tanese, H. S. Nguyen, H. Flayac, E. Galopin, A. Lemaître, I. Sagnes, D. Solnyshkov, A. Amo, G. Malpuech, J. Bloch, All-optical phase modulation in a cavity-polariton Mach-Zehnder interferometer. *Nat. Commun.* **5**, 3278 (2014).
6. A. Imamoglu, R. J. Ram, S. Pau, Y. Yamamoto, Nonequilibrium condensates and lasers without inversion: Exciton-polatiron laser. *Phys. Rev. A* **53**, 4250–4253 (1996).
7. C. Schneider, A. Rahimi-Iman, N. Y. Kim, J. Fischer, I. G. Savenko, M. Amthor, M. Lermer, A. Wolf, L. Worschech, V. D. Kulakovskii, I. A. Shelykh, M. Kamp, S. Reitzenstein, A. Forchel, Y. Yamamoto, S. Höfling, An electrically pumped polariton laser. *Nature* **497**, 348–352 (2013).
8. R. Colombelli, J.-M. Manceau, Perspective for intersubband polariton laser. *Phys. Rev. X* **5**, 011031 (2015).
9. P. Li, X. Yang, T. W. W. Maβ, J. Hanss, M. Lewin, A.-K. U. Michel, M. Wuttig, T. Taubner, Reversible optical switching of highly confined phonon-polaritons with an ultrathin phase-change material. *Nat. Mater.* **15**, 870–876 (2016).
10. H. Huebl, C. W. Zollitsch, J. Lotze, F. Hocke, M. Greifenstein, A. Marx, R. Gross, S. T. B. Goennenwein, High cooperativity in coupled microwave resonator ferromagnetic insulator hybrids. *Phys. Rev. Lett.* **111**, 127003 (2013).
11. Y. Tabuchi, S. Ishino, T. Ishikawa, R. Yamazaki, K. Usami, Y. Nakamura, Hybridizing ferromagnetic magnons and microwave photons in the quantum limit. *Phys. Rev. Lett.* **113**, 083603 (2014).
12. D. L. Mills, E. Burstein, Polaritons: The electromagnetic modes of media. *Rep. Prog. Phys.* **37**, 817–926 (1974).
13. C. H. Henry, J. J. Hopfield, Raman scattering by polaritons. *Phys. Rev. Lett.* **15**, 964–966 (1965).
14. J. M. Yarborough, S. S. Sussman, H. E. Purhoff, R. H. Pantell, B. C. Johnson, Efficient, tunable optical emission from $LiNbO_3$ without a resonator. *Appl. Phys. Lett.* **15**, 102–105 (1969).
15. K. Kawase, M. Sato, T. Taniuchi, H. Ito, Coherent tunable THz wave generation from $LiNbO_3$ with monolithic grating coupler. *Appl. Phys. Lett.* **68**, 2483–2485 (1996).
16. J.-J. Greffet, R. Carminati, K. Joulain, J.-P. Mulet, S. Mainguy, Y. Chen, Coherent emission of light by thermal sources. *Nature* **416**, 61–64 (2002).
17. T. Feurer, J. C. Vaughan, K. A. Nelson, Spatiotemporal coherent control of lattice vibrational waves. *Science* **299**, 374–377 (2003).
18. N. S. Stoyanov, D. W. Ward, T. Feurer, K. A. Nelson, Terahertz polariton propagation in patterned materials. *Nat. Mater.* **1**, 95–98 (2002).
19. D. J. Shelton, I. Brener, J. C. Ginn, M. B. Sinclair, D. W. Peters, K. R. Coffey, G. D. Boreman, Strong coupling between nanoscale metamaterials and phonons. *Nano Lett.* **11**, 2104–2108 (2011).
20. S. Dai, Z. Fei, Q. Ma, A. S. Rodin, M. Wagner, A. S. McLeod, M. K. Liu, W. Gannett, W. Regan, K. Watanabe, T. Taniguchi, M. Thiemens, G. Dominguez, A. H. Castro Neto, A. Zettl, F. Keilmann, P. Jarillo-Herrero, M. M. Fogler, D. N. Basov, Tunable phonon polaritons in atomically thin van der Waals crystals of Boron Nitride. *Science* **343**, 1125–1129 (2014).
21. J. Faist, F. Capasso, D. L. Sivco, C. Sirtori, A. L. Hutchinson, A. Y. Cho, Quantum cascade laser. *Science* **264**, 553–556 (1994).
22. J. Faist, M. Beck, T. Aellen, E. Gini, Quantum-cascade lasers based on a bound-to-continuum transition. *Appl. Phys. Lett.* **78**, 147–149 (2001).
23. R. Terazzi, J. Faist, A density matrix model of transport and radiation in quantum cascade lasers. *New J. Phys.* **12**, 033045 (2010).
24. M. Franckié, C. Ndebeka-Bandou, K. Ohtani, J. Faist, Quantum model of gain in phonon-polariton lasers. *Phys. Rev. B* **97**, 075402 (2018).
25. A. Wacker, M. Lindskog, D. O. Winge, Nonequilibrium Green's function model for simulation of quantum cascade laser devices under operating conditions. *IEEE J. Sel. Top. Quantum Electron.* **19**, 1200611 (2013).
26. K. Unterrainer, R. Colombelli, C. Gmachl, F. Capasso, H. Y. Hwang, A. Sergent, A. Michael, D. L. Sivco, A. Y. Cho, Quantum cascade lasers with double metal-semiconductor waveguide resonators. *Appl. Phys. Lett.* **80**, 3060–3062 (2002).
27. H. Ding, G. Weihs, C. Santori, J. Bloch, Y. Yamamoto, Condensation of semiconductor microcavity exciton polaritons. *Science* **298**, 199–202 (2002).
28. H. Ding, G. Weihs, D. Snoke, J. Bloch, Y. Yamamoto, Polariton lasing vs. photon lasing in a semiconductor microcavity. *Proc. Natl. Acad. Sci. U.S.A.* **100**, 15318–15323 (2003).
29. K. Ohtani, M. Beck, M. J. Süess, J. Faist, A. M. Andrews, T. Zederbauer, H. Detz, W. Schrenk, G. Strasser, Far-infrared quantum cascade lasers operating in AlAs phonon reststrahlen band. *ACS Photonics* **3**, 2280–2284 (2016).
30. R. Houdré, C. Weisbuch, R. P. Stanley, U. Oesterle, P. Pellandini, M. Ilegems, Measurement of cavity-polariton dispersion curve from angle-resolved photoluminescence experiments. *Phys. Rev. Lett.* **73**, 2043–2046 (1994).
31. Y. Todorov, C. Sirtori, Intersubband polaritons in the electrical dipole gauge. *Phys. Rev. B* **85**, 045304 (2012).
32. H. Chu, Y.-C. Chang, Phonon-polariton modes in superlattices: The effect of spatial dispersion. *Phys. Rev. B* **38**, 12369–12376 (1988).
33. J. J. Hopfield, Theory of the contribution of excitons to the complex dielectric constant of crystals. *Phys. Rev.* **112**, 1555–1567 (1958).
34. S. S. Dhillon, C. Sirtori, J. Alton, S. Barbieri, A. De Rossi, H. E. Beere, D. A. Ritchie, Terahertz transfer onto a telecom optical carrier. *Nat. Photonics* **1**, 411–415 (2007).
35. S. Houver, P. Cavalié, M. R. St-Jean, M. I. Amanti, C. Sirtori, L. H. Li, A. G. Davies, E. H. Linfield, T. A. S. Pereira, A. Lebreton, J. Tignon, S. S. Dhillon, Optical sideband

generation up to room temperature with mid-infrared quantum cascade lasers. *Opt. Express* **23**, 4012–4019 (2015).
36. M. Giehler, E. Jahna, K. Ploog, Linewidth of phonon modes in infrared transmission spectra of GaAs/AlAs superlattices. *J. Appl. Phys.* **77**, 3566–3568 (1995).
37. K. Ohtani, C. Ndebeka-Bandou, L. Bosco, M. Beck, J. Faist, A quantum cascade phonon-polariton laser. arXiv:1610.00963 [physics.optics] (4 October 2016).
38. A. Debernardi, Phonon linewidth in III-V semiconductors from density-functional perturbation theory. *Phys. Rev. B* **57**, 12847–12858 (1998).
39. K. Vahala, M. Herrmann, S. Knünz, V. Batteiger, G. Saathoff, T. W. Hänsch, T. Udem, A phonon laser. *Nat. Phys.* **5**, 682–686 (2009).
40. I. Mahboob, K. Nishiguchi, A. Fujiwara, H. Yamaguchi, Phonon lasing in an electromechanical resonator. *Phys. Rev. Lett.* **110**, 127202 (2013).
41. J. Chen, J. B. Khurgin, Feasibility analysis of phonon lasers. *IEEE J. Quantum Electron.* **39**, 600–607 (2003).
42. J. B. Khurgin, S. Bajaj, S. Rajan, Amplified spontaneous emission of phonons as a likely mechanism for density-dependent velocity saturation in GaN transistor. *Appl. Phys. Express* **9**, 094101 (2016).
43. J. D. Caldwell, L. Lindsay, V. Giannini, I. Vurgaftman, T. L. Reinecke, S. A. Maier, O. J. Glembocki, Low-loss, infrared and terahertz nanophotonics using surface phonon polaritons. *Nanophotonics* **4**, 44–68 (2014).
44. A. J. Giles, S. Dai, I. Vurgaftman, T. Hoffman, S. Liu, L. Lindsay, C. T. Ellis, N. Assefa, I. Chatzakis, T. L. Reinecke, J. G. Tischler, M. M. Fogler, J. H. Edgar, D. N. Basov, J. D. Caldwell, Ultra-low loss polaritons in isotopically pure boron nitride. *Nat. Mater.* **17**, 134–139 (2018).
45. M. Cardona, Light scattering in solids II, in *Topics in Applied Physics*, M. Cardona, G. Güntherodts, Eds. (Springer, Berlin, 1982), vol. 50, pp. 19–178.
46. C. Deutsch, M. Krall, M. Brandstetter, H. Detz, A. M. Andrews, P. Klang, W. Schrenk, G. Strasser, K. Unterrainer, High performance InGaAs/GaAsSb terahertz quantum cascade lasers operating up to 142 K. *Appl. Phys. Lett.* **101**, 211117 (2012).
47. G. Scamarcio, L. Tapfer, W. König, A. Fischer, K. Ploog, E. Molinari, S. Baroni, P. Giannozzi, D. de Gironcoli, Infrared reflectivity by transverse-optical phonons in $(GaAs)_m/(AlAs)_n$ ultrathin-layer superlattices. *Phys. Rev. B* **43**, 14754–14757 (1991).
48. O. Madelung, U. Rössler, M. Schulz, Indium arsenide (InAs) dielectric constants, in *Group IV Elements, IV-IV and III-V Compounds. Part A – Lattice Properties* (Springer Berlin Heidelberg, 2001) pp. 1–3.
49. D. J. Lockwood, G. Yu, N. L. Rowell, Optical phonon frequencies and damping in AlAs, GaP, GaAs, InP, InAs and InSb studied by oblique incidence infrared spectroscopy. *Solid State Commun.* **136**, 404–409 (2005).
50. O. Madelung, U. Rössler, M. Schulz, Aluminum arsenide (AlAs) dielectric constants, in *Group IV Elements, IV-IV and III-V Compounds. Part A - Lattice Properties* (Springer Berlin Heidelberg, 2001) pp. 1–4.
51. M. A. Ordal, R. J. Bell, R. W. Alexander Jr., L. L. Long, M. R. Querry, Optical properties of fourteen metals in the infrared and far infrared: Al, Co, Cu, Au, Fe, Pb, Mo, Ni, Pd, Pt, Ag, Ti, V and W. *Appl. Opt.* **24**, 4493–4499 (1985).
52. A. Fainstein, P. Etchegoin, M. P. Chamberlain, M. Cardona, K. Tötemeyer, K. Eber, Selection rules and dispersion of GaAs/AlAs multiple-quantum-well optical phonons studied by Raman scattering in right-angle, forward, and backscattering in-plane geometries. *Phys. Rev. B* **51**, 14448–14458 (1995).
53. L. Bosco, C. Bonzon, K. Ohtani, M. Justen, M. Beck, J. Fast, A patch-array antenna single-mode low electrical dissipation continuous wave terahertz quantum cascade laser. *Appl. Phys. Lett.* **109**, 201103 (2016).

Acknowledgments: We acknowledge discussions with A. Vasanelli, S. d. Liberato, and J. B. Khurgin and also thank A. M. Andrews, T. Zederbauer, H. Detz, W. Schrenk, and G. Strasser for supporting MBE growth of InGaAs/GaAsSb material at early stage of this work. **Funding:** The presented work was supported in part by the ERC Advanced grant Quantum Metamaterials in the ultrastrong coupling regime (MUSiC) with the ERC grant no. 340975, as well as by the Swiss National Science Foundation (SNF) through the National Center of Competence in Research Quantum Science and Technology (NCCR QSIT). **Author contributions:** K.O. designed all structures, conducted the MBE growth of Sb-based material, the computation of the theoretical polariton dispersion and dielectric function calculations, the device characteristics, and the low-temperature Raman scattering experiment under biasing. B.M. conducted recent Raman experiments, and L.B. processed the grown structures into laser devices. M.F., C.N.-B., and J.F. developed the theoretical framework and software for the phonon-polariton gain calculations. M.B. performed MBE growth of the Sb-free structures. K.O. and J.F. had the original idea and drafted the initial manuscript. M.F. and B.M. performed the reviewing and editing. Last, J.F. supervised this work. **Competing interests:** The authors declare that they have no competing interests. **Data and materials availability:** All data needed to evaluate the conclusions in the paper are present in the paper and/or in the Supplementary Materials. The measured samples and the codes used to generate the theoretical data are available at ETH Zürich. Additional data related to this paper may be requested from the authors.

Submitted 13 May 2018
Accepted 5 June 2019
Published 12 July 2019
10.1126/sciadv.aau1632

Citation: K. Ohtani, B. Meng, M. Franckié, L. Bosco, C. Ndebeka-Bandou, M. Beck, J. Faist, An electrically pumped phonon-polariton laser. *Sci. Adv.* **5**, eaau1632 (2019).

An electrically pumped phonon-polariton laser

Keita Ohtani, Bo Meng, Martin Franckié, Lorenzo Bosco, Camille Ndebeka-Bandou, Mattias Beck and Jérôme Faist

Sci Adv **5** (7), eaau1632.
DOI: 10.1126/sciadv.aau1632